Nano Energy 88 (2021) 106307

Contents lists available at ScienceDirect

Nano Energy

journal homepage: www.elsevier.com/locate/nanoen

One-stone, two birds: Alloying effect and surface defects induced by Pt on $Cu_{2-x}Se$ nanowires to boost C-C bond cleavage for electrocatalytic ethanol oxidation

Hongcheng Peng [a,1], Jun Ren [b,1], Yuchao Wang [a,1], Yu Xiong [a], Qichen Wang [a], Qian Li [a], Xin Zhao [a], Longsheng Zhan [a], Lirong Zheng [c], Yougen Tang [a], Yongpeng Lei [a,*]

[a] State Key Laboratory of Powder Metallurgy, Hunan Provincial Key Laboratory of Chemical Power Sources, College of Chemistry and Chemical Engineering, Central South University, Changsha 410083, China
[b] College of Chemical Engineering and Environment, North University of China, Taiyuan 030051, China
[c] Beijing Synchrotron Radiation Facility, Institute of High Energy Physics, Chinese Academy of Sciences, Beijing 100049, China

ARTICLE INFO

Keywords:
Metal-support interaction
Selenides
Surface defects
Alloying
C-C bond cleavage
Ethanol oxidation reaction

ABSTRACT

The high-efficient C-C bond cleavage is the key for ethanol electrooxidation. In this work, PtCu/$Cu_{2-x}Se$ nanowires (NWs) with abundant surface defects were constructed and exhibited remarkable activity of 5.03 A mg^{-1}_{Pt} as well as 5.29 A mg^{-1}_{Pt} for ethanol oxidation and methanol oxidation, respectively, which are 5.0 and 5.3 fold of commercial Pt/C. ex situ, in situ experiments and calculation results reveal that the formation of PtCu alloys lowered the D-band level to promote the adsorption of hydroxyl species. The abundant defects created high density of low-coordinated atoms to boost the reaction kinetics. Thus, PtCu/$Cu_{2-x}Se$ NWs displayed enhanced C-C bond cleavage ability and high selectivity for C1 products (CO_2). The assembled direct ethanol fuel cells (DEFCs) with PtCu/$Cu_{2-x}Se$ NWs as anode provided an open-circuit voltage (OCV) of 0.773 V and a peak power density of 7.8 mW cm^{-2}. This work not only give us a potential catalyst for C-C bond cleavage, but also provides an effective strategy to enhance the electrocatalytic activity of ethanol/methanol oxidation.

1. Introduction

Direct alcohol fuel cells (DAFCs), including direct ethanol fuel cells (DEFCs) and direct methanol fuel cells (DMFCs), etc., are very promising power sources because of the high energy density of liquid fuels (8.01 kWh kg^{-1} for ethanol and 6.07 kWh kg^{-1} for methanol), mild working temperature and low emission of pollutants [1–3]. Though Pt-based catalysts for ethanol and methanol oxidation reaction (EOR and MOR) are effective, the low abundance of Pt impedes the commercialization [4]. Enormous efforts have been paid to reduce the usage of Pt while not lower the catalytic performance. Alloying Pt with low-priced metals and constructing precising nanostructure are the major strategies [5–7]. Moreover, the sluggish alcohol oxidation kinetics and CO-like carbonaceous intermediates poisoning restrict the efficiency of EOR and MOR. For EOR, two reaction pathway exists: the incomplete oxidation of ethanol to acetic acid or acetate with 4 electrons transfer (C2 pathway) and the complete oxidation of ethanol to CO_2 with 12 electrons transfer (C1 pathway). Particularly, due to C1 pathway's high energy of C-C bond cleavage, it is challenging to enhance the reaction kinetics.

As known, rational supported catalysts with strong metal-support interactions (MSIs) could bring new catalytic phenomena by electron transfer [8,9], interfacial condition [10], morphologies and composition regulation [11]. Liang et al. [12] reported the Ce-modified Pt NPs for MOR. The Cerium (III) oxygenated species dispersed on Pt NPs interacted with Pt atoms to enhance the MOR performance. Chen et al. [13] developed a porous Pd-PdO nanotubes for MOR. The electronic effect and bifunctional mechanism between PdO and Pd decreased the reaction activation energy of MOR. It is noted that copper selenides possess multiple crystal phases, such as stoichiometric (i.e., CuSe, Cu_2Se, Cu_2Se_3) and nonstoichiometric ($Cu_{2-x}Se$) phases [14]. With multiple oxidation states, the unsaturated Cu atoms on edge/surface of $Cu_{2-x}Se$ phase favor more exposed active sites [15,16]. Furthermore, to enhance the catalytic reactivity, defect engineering has been proved as an efficient strategy for electronic structure tuning and surface /interface

* Corresponding author.
E-mail address: leiyongpeng@csu.edu.cn (Y. Lei).
[1] These authors contributed equally to this work.

https://doi.org/10.1016/j.nanoen.2021.106307
Received 31 May 2021; Received in revised form 21 June 2021; Accepted 28 June 2021
Available online 1 July 2021

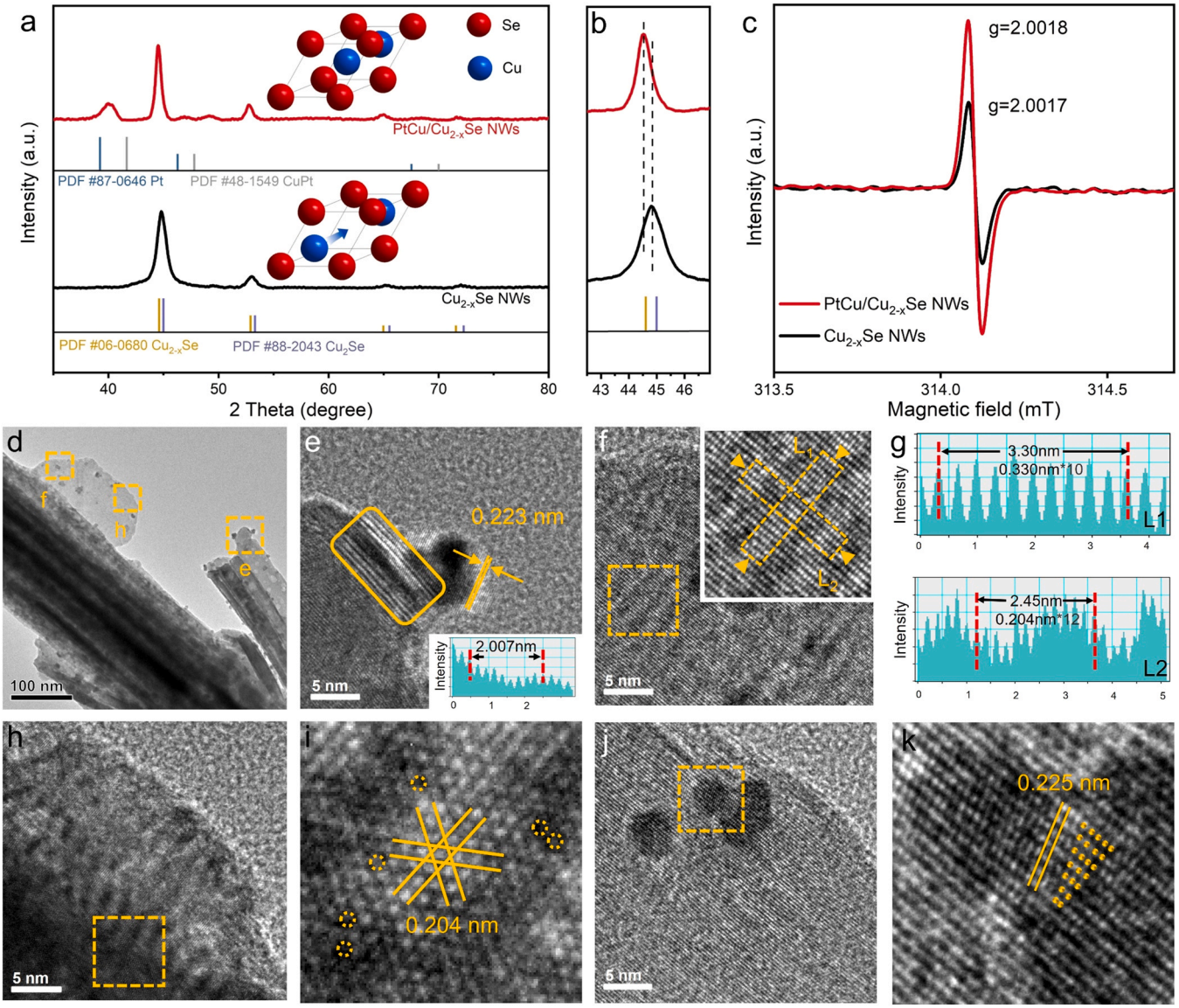

Fig. 1. (a) XRD patterns, (b) amplified patterns and (c) EPR spectra of PtCu/$Cu_{2-x}Se$ NWs and $Cu_{2-x}Se$ NWs. (d) TEM image of PtCu/$Cu_{2-x}Se$ NWs. (e, f, h) HRTEM images of yellow square region in (d). (g) Line intensity profile taken along L1 and L2 direction. (i) The amplified HRTEM image of yellow square region in (h). (j) HRTEM image of PtCu NPs with surface defects. (k) The amplified HRTEM image of yellow square region in (j).

modulation [17–19].

Herein, on $Cu_{2-x}Se$, a one-stone, two birds strategy of forming PtCu alloys to low the d-band center of Pt and producing more defects to create high density of low-coordinated atoms was demonstrated. The obtained PtCu/$Cu_{2-x}Se$ NWs catalyst exhibited 5.0 and 5.3 fold current densities for EOR and MOR in alkaline solution than that of commercial Pt/C, respectively. Combined with ex situ, in situ experiments and calculation results, PtCu/$Cu_{2-x}Se$ NWs displayed a higher efficiency to drive C-C bond cleavage than that of commercial Pt/C.

2. Results and discussion

PtCu/$Cu_{2-x}Se$ NWs were synthesized by self-assembly of CuSe nanoplates and subsequent Pt^{4+} precursor's reduction (Scheme S1) [20]. In the X-ray diffraction (XRD) patterns (Fig. 1a), the diffraction peaks of $Cu_{2-x}Se$ NWs located between Cu_2Se (JCPDS No. 88–2043) and $Cu_{2-x}Se$ phase (JCPDS No. 06-0680). After Pt^{4+} precursor was reduced and deposited on $Cu_{2-x}Se$ NWs, the characteristic peaks between Pt (JCPDS No. 87–0646) and PtCu (JCPDS No. 48-1549) emerged. The introduction of Pt activated the Cu^{2+} cation, so the Cu atoms diffuse to the Pt NPs and form PtCu alloy [11]. The amplified image (Fig. 1b) shows that the characteristic peak at 2θ of 44.8° occurred a slight left shift, and nearly coincided to $Cu_{2-x}Se$ phase. It explains that the Cu atoms among PtCu alloy stem from $Cu_{2-x}Se$ NWs. The isotropic electron paramagnetic resonance (EPR) signals at $g = 2.0017$ in Fig. 1c were observed, which should be ascribed to the hole trapped on some highly symmetric center [21]. In consideration of the unpaired Cu atoms on the surface of $Cu_{2-x}Se$ NWs, the EPR signal could be bound to Cu vacancies [22]. The intensity of EPR signal was obviously enhanced due to the increasing amount of vacancies [23]. Combining with the XRD analysis above, we can conclude that the Cu atoms on the surface of $Cu_{2-x}Se$ diffused and alloyed with Pt atoms to increase the surface defects concentration.

Fig. 1d illustrates the overall TEM image of PtCu/$Cu_{2-x}Se$ NWs with a diameter of about 200 nm. As seen, $Cu_{2-x}Se$ NWs were composed of numerous thin bundles. The magnified TEM images (Fig. S1a and b) show that there were plenty of ditches in the middle of NWs and steps at ends, which were attributed to the water evaporation-induced mechanism of $Cu_{2-x}Se$ NWs. And some nanoplates that were not assembled into bundles, lie on the rim of NWs. This unique one-dimensional

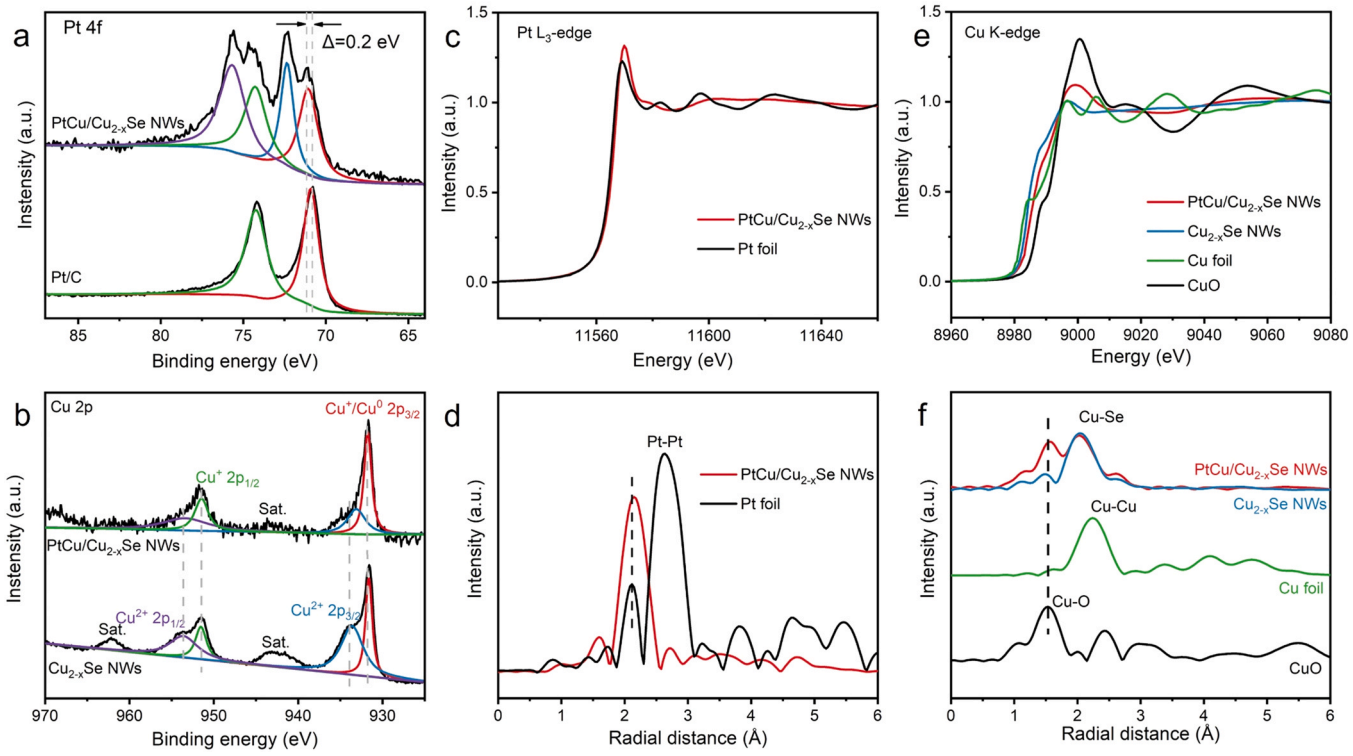

Fig. 2. (a) High-resolution Pt 4f and (b) Cu 2p XPS spectra of PtCu/Cu_{2-x}Se NWs and Cu_{2-x}Se NWs. (c) The normalized XANES at Pt L_3-edge and (d) corresponding FT-EXAFS spectra of (c). (e) The normalized XANES at Cu K-edge and (f) corresponding FT-EXAFS spectra of (e).

nanostructure exposes more active sites for PtCu NPs, and provides rapid transport channel for electrons and intermediates. In the high-resolution TEM (HRTEM) image (Fig. 1e), the PtCu NPs can be observed clearly. The lattice spacing of 0.223 and 0.193 nm belonged to PtCu (200) and (111) planes, respectively (Fig. S1e). Following Vegard's law [24], the Pt/Cu atomic ratio was calculated to be 2:1. Fig. 1f and h give the crystal lattice arrangement of Cu_{2-x}Se viewed along different orientation. The amplified image in the yellow frame region (Fig. 1f) displayed good crystallinity. The line intensity profile taken along L1 and L2 direction exhibited the lattice spacing of 0.330 and 0.204 nm, which were assigned to Cu_{2-x}Se (111) and (200) planes, respectively (Fig. 1g). For Cu_{2-x}Se NWs (Fig. S1c and d), the lattice spacing of 0.203 nm corresponded to Cu_{2-x}Se (200) planes, and the lattice spacing of 0.324 and 0.333 nm corresponded to Cu_{2-x}Se (111) planes. This nuance maybe stem from distortion caused by lattice compression. Fig. 1h shows the support situation of PtCu/Cu_{2-x}Se NWs. The corresponding fast Fourier transform (FFT) patterns (Fig. S2) show that, as Pt introducing into the Cu_{2-x}Se NWs, the crystal structure transformed from *Fm-3m* to *F-43m*, exactly as the lattice diagram listed in Fig. 1a. It confirms the diffusion of Cu atoms from nanoscale level. Thus, we propose that the surface defects originated by the diffusion of Cu atoms from Cu_{2-x}Se NWs to PtCu NPs. The surface defects on PtCu/Cu_{2-x}Se NWs can be divided into three species: stacking faults led by Shockley partial dislocation (Fig. 1e and S1c) [25,26], Cu vacancies (Fig. 1i) [27], and plane defects led by small-angle grain boundaries (Fig. 1k). As Pt deposited on Cu_{2-x}Se NWs, these defects tended to gather on the interface, which may be due to two aspects. First, alloying with Pt could increase the lattice mismatch of surface atoms. Second, the tensile strain derived from the Pt facilitated the generation of defects [28].

The Pt, Cu, Se and O elements were observed in the X-ray photoelectron spectroscopy (XPS) of PtCu/Cu_{2-x}Se NWs (Fig. S3). The Pt 4f spectra could be deconvoluted into two spin-orbit doublets (Fig. 2a). Compared to the Pt $4f_{7/2}$ peak of Pt/C, the fitting peak at binding energy of 71.3 eV shift to the left by 0.2 eV. It indicated that Pt carried positive charge through electron transfer from PtCu NPs to Cu_{2-x}Se NWs [29, 30]. The electron tuning will lower the D-band center of Pt, which contributed to the adsorption of O_{ad} and OH_{ad} species on Pt atoms to improve intrinsic activity [31]. The fitting peaks at binding energies of 75.7 and 72.4 eV were regarded as Pt oxidation states [32]. In the high-resolution Cu 2p spectra of Cu_{2-x}Se NWs (Fig. 2b), the Cu $2p_{1/2}$ and $2p_{3/2}$ peaks at 951.5 and 931.6 eV were attributed to Cu^+. And the peaks at 953.6 and 933.6 eV were attributed to the Cu^{2+}. As the Pt metal deposited on Cu_{2-x}Se NWs, the intensity of peak corresponding to Cu^{2+} was obviously weaker. And the peaks at 951.5 and 931.6 eV were inferred to metallic Cu and Cu^+. The reduction of Cu^{2+} supports the formation of PtCu alloy, in accordance with the HRTEM results above [33,34].

The X-ray absorption near-edge structure (XANES) spectroscopy and extended X-ray absorption fine structure (EXAFS) spectroscopy were measured to further investigate the electronic structure and coordination information. The white line intensity of PtCu/Cu_{2-x}Se NWs is higher than that of Pt foil, suggesting a positive valence state of Pt atoms (Fig. 2c) [35], consistent with XPS results. For Cu K-edge XANES spectrum, the formation of PtCu alloy obviously improved the white line intensity, and the valence state of Cu in PtCu/Cu_{2-x}Se NWs is between divalent and zero valence (Fig. 2e). The EXAFS oscillation curves at Pt L_3-edge and Cu K-edge are presented in Fig. S4. In the corresponding Fourier-transformed EXAFS (FT-EXAFS) spectra (Fig. 2d), the Pt-Pt bonds at 2.63 Å and 2.11 Å of Pt foil can be observed. Simultaneously, the strong peak at 2.15 Å of PtCu/Cu_{2-x}Se NWs indicated the overlapping of both Pt-Pt and Pt-Cu coordination, resulting from the formation of PtCu alloy [36–38]. Fig. 2f exhibits the FT-EXAFS spectra of Cu K-edge. It can be found that the Cu atoms mainly coordinate with Se atoms (peak at 2.04 Å) in Cu_{2-x}Se NWs and PtCu/Cu_{2-x}Se NWs. By introducing Pt species onto Cu_{2-x}Se NWs, the peak intensity dropped down, which suggested the new generation of Cu defects [39]. And this peak occurred a slight negative shift, which may be due to the structural lattice shrinkage of Cu-Se bonds [35]. Besides, a new coordination peak at 1.56 Å corresponding to Cu-O bonds appeared, which should be originated from the surface oxidation of PtCu/Cu_{2-x}Se NWs. The

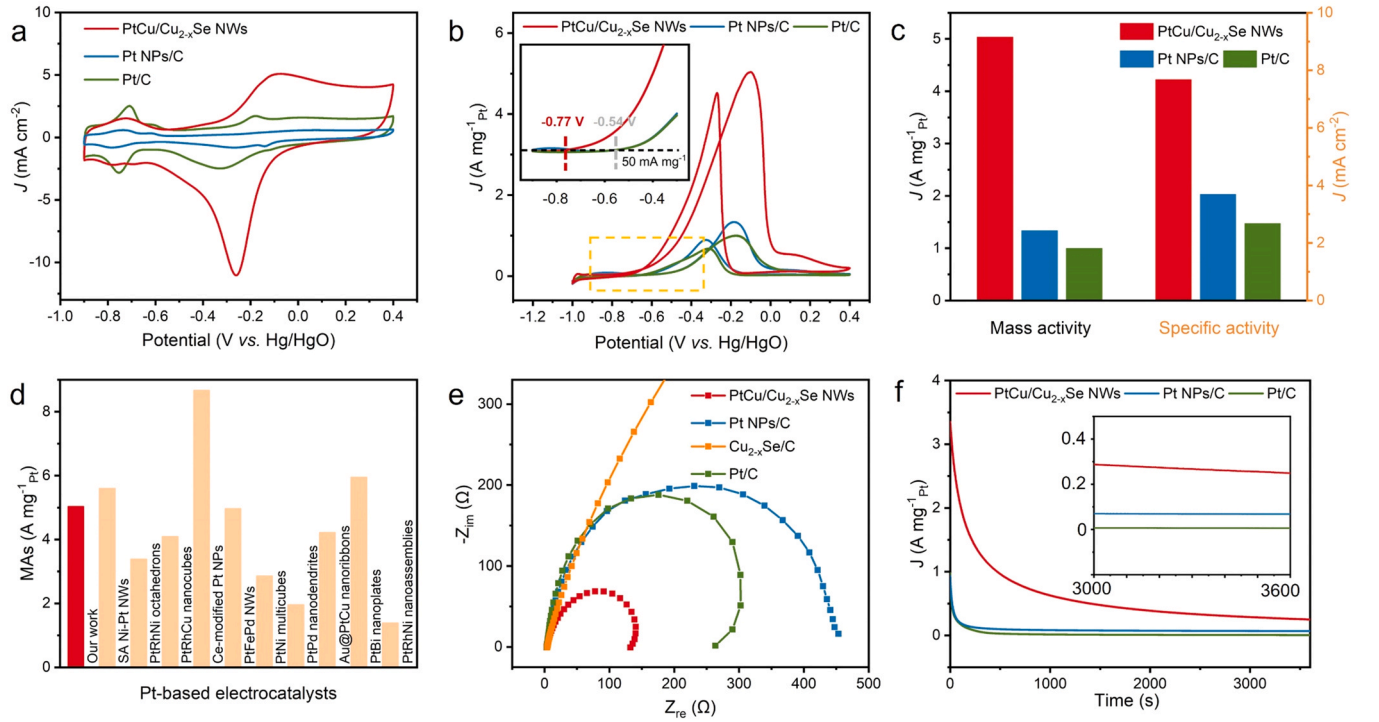

Fig. 3. CV curves in (a) 1.0 M KOH, and (b) 1.0 M KOH and 1.0 M ethanol solution (scanning rate: 50 mV s^{-1}). (c) MAs and SAs. (d) EOR MAs of recent reported Pt-based catalysts. (references listed in Supporting information) (e) Nyquist plots measured at −0.4 V in 1.0 M KOH and 1.0 M ethanol electrolyte. (f) CA curves at −0.2 V.

electronic structure of Se was investigated by XPS and XAFS characterization (Fig. S5). The description was given in Supporting information.

The electrochemical performance was measured in a three-electrode system. In the cyclic voltammetry (CV) curves of PtCu/Cu_{2-x}Se NWs (Fig. 3a), there was a board peak between −0.2 and 0 V in the forward scan, which referred to Cu atoms dissolving process from the Cu_{2-x}Se NWs [40]. In the backward scan, a PtO reduction peak at approximately −0.2 V appeared, which represented the hydroxyl adsorption on the surface of Pt [41]. According to the mass percentage of Pt in different samples (Table S1), the electrochemically active surface area (ECSA) of PtCu/Cu_{2-x}Se NWs was calculated to be 65.5 m^2 g^{-1}, much larger than those of Pt NPs/C (36.1 m^2 g^{-1}) and commercial Pt/C (37.1 m^2 g^{-1}). The Pt NPs/C sample was prepared in the same method except replacing the Cu_{2-x}Se NWs with the same weight of carbon black. The double-layer capacitance (C_{dl}) measurements (Fig. S6) showed the large electrochemical reaction area and more active sites. Then the electrolyte was replaced with 1.0 M KOH and 1.0 M ethanol, two peaks at forward and backward scan emerged promptly (Fig. 3b). For PtCu/Cu_{2-x}Se NWs, the peak potential of ethanol oxidation was shifted positively relative to Pt NPs/C and commercial Pt/C, which could attribute to the formation of PtCu alloy [42]. The forward peak corresponded to the oxidation of ethanol, and the backward peak corresponded to the oxidation of intermediate products. Since the CV curves of bare Cu_{2-x}Se NWs were narrow (Fig. S7), the activity contribution mainly came from PtCu. The mass activities (MAs) were normalized to the mass fraction of Pt. PtCu/Cu_{2-x}Se NWs showed highest MA with a current density of 5.03 A mg^{-1}_{Pt} @−0.10 V, which was 3.8 and 5.0 fold of Pt NPs/C (1.33 A mg^{-1}_{Pt} @ −0.18 V) and commercial Pt/C (0.99 A mg^{-1}_{Pt} @ −0.17 V), respectively (Fig. 3c). The PtCu/Cu_{2-x}Se NWs displayed a relatively high MA among the recently reported Pt-based catalysts (Fig. 3d). The other Pt-based catalysts are listed in detail in Table S4. Moreover, PtCu/Cu_{2-x}Se NWs showed a more negative onset potential (~230 mV, defined as the potential required to reach a MA of 50 mA mg^{-1}_{Pt}) than Pt NPs/C and Pt/C. The results indicate that the easier formation of hydroxyl on the PtCu/Cu_{2-x}Se surface favored ethanol oxidation [43]. The negative shift of onset overpotential could ascribe to the modified surface electronic structure [44]. Besides, the specific activities (SAs) normalized to ESCAs were measured to be 7.68, 3.69, and 2.68 mA cm^{-2} for PtCu/Cu_{2-x}Se NWs, Pt NPs/C, and commercial Pt/C catalysts, respectively (Fig. 3c).

In the Nyquist plots (Fig. 3e), for PtCu/Cu_{2-x}Se NWs, the smallest diameter of impedance arc implied the lowest charge transfer resistance and highest reaction rate on catalyst surface. The forward linear sweep voltammetry (LSV) with a scan rate of 10 mV s^{-1} was obtained as a quasi-steady-state condition, and the current was normalized peak value (Fig. S8a). The PtCu/Cu_{2-x}Se NWs showed a much better activity at lower overpotential. In Fig. S8b, PtCu/Cu_{2-x}Se NWs exhibited the smallest Tafel slope, suggesting that the fastest charge- and mass-transfer kinetics of EOR. On one hand, PtCu/Cu_{2-x}Se NWs with abundant surface defects and tensile strain have a high density of low-coordinated atoms [45]. On the other hand, alloying Pt with Cu could lower the Pt d-band level and promote the adsorption of hydroxyl species.

The chronoamperometry (CA) curves were performed (Fig. 3f). In the initial stage, all curves declined rapidly because of the formation of CO-like intermediates, which adsorb on the Pt active sites and obstruct the further EOR [46]. PtCu/Cu_{2-x}Se NWs exhibited a slower current decay rate than other two catalysts. Gradually, all curves reached a stable state while PtCu/Cu_{2-x}Se NWs stayed a highest current density. The alloying with Cu downshifted the d-band center of Pt, which could weaker adsorption of CO on PtCu/Cu_{2-x}Se NWs and improve the oxidation of CO [47]. After 1 h electrolyzing, PtCu/Cu_{2-x}Se NWs still remained 250 mA mg^{-1}_{Pt}, far higher than that of Pt NPs/C (68 mA mg^{-1}_{Pt}) and commercial Pt/C (8 mA mg^{-1}_{Pt}). In addition, we performed a consecutive 500 cycles of CV tests to further test the stability (Fig. S9). At first 200 cycles, PtCu/Cu_{2-x}Se NWs and commercial Pt/C remained almost the same normalized current. After 200th cycle, the decline rate of PtCu/Cu_{2-x}Se NWs turned smoothly. To explain this phenomenon, we analyzed the TEM images of PtCu/Cu_{2-x}NWs at 200th

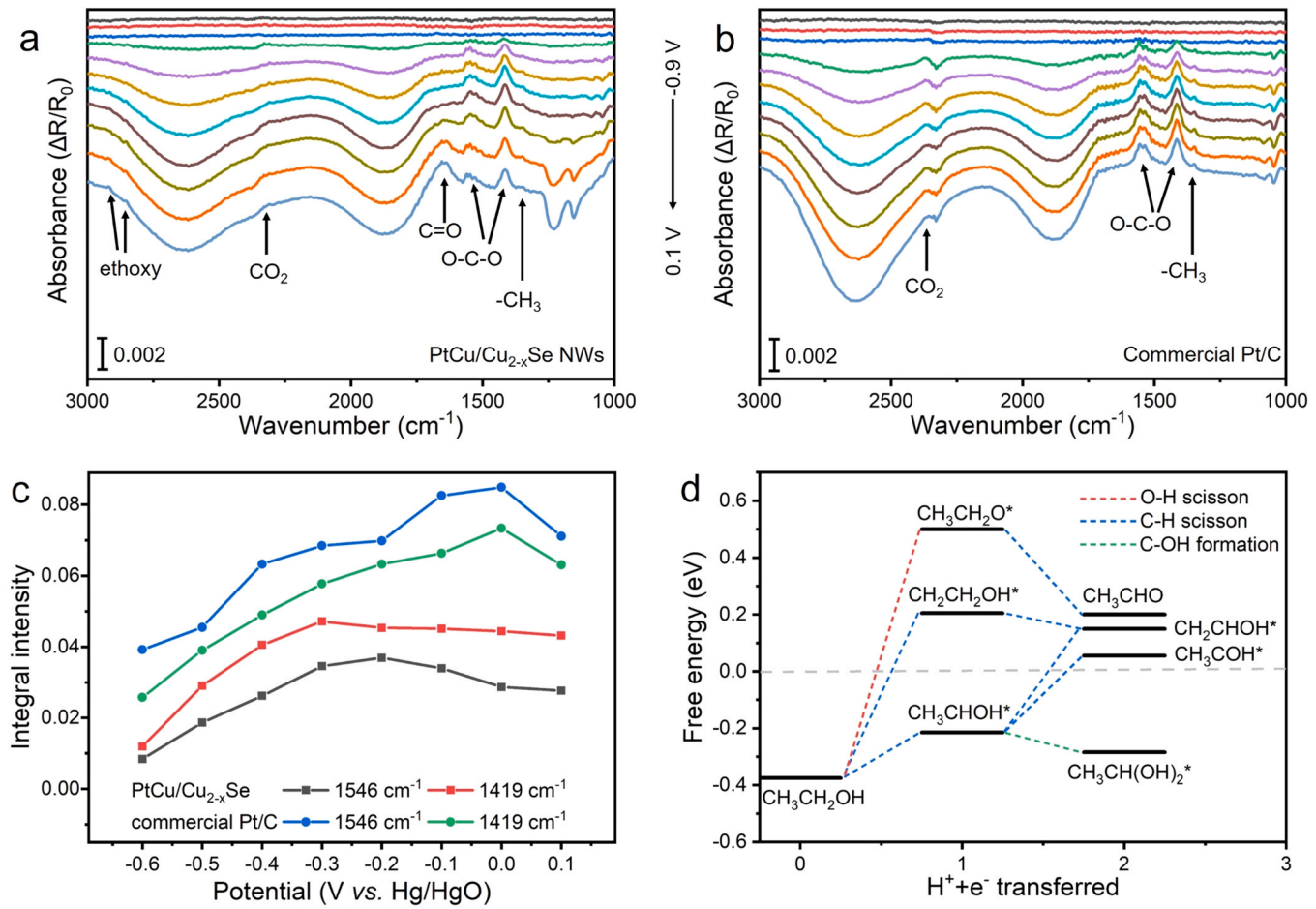

Fig. 4. in situ FTIR spectra of (a) PtCu/Cu_{2-x}Se NWs and (b) commercial Pt/C with a step of 100 mV in 1.0 M KOH and 1.0 M ethanol solution (reference potential E_R is −1.0 V). (c) Integral in situ FTIR intensities at 1545 and 1419 cm^{-1}. (d) Reaction energy profile of intermediates for ethanol oxidation toward CH_3COO^-.

and 500th CV cycle (Fig. S10). The acitivies loss was mainly owing to the volume expansion of selenide [48]. The Raman spectra of PtCu/Cu_{2-x}Se NWs before and after EOR electrolyzing were shown in Fig. S11. The vibration modes of 181 and 212 cm^{-1} were ascribed to Se-Se stretching mode [49]. The full width at half maximum of peak at 212 cm^{-1} were narrower after EOR electrolyzing, which suggested that the lattice distortion was decreasing. These are the major reasons for the catalytic activity of Pt/Cu_{2-x}Se NWs catalyst going down. Due to the multiple dehydrogenation and oxidation of ethanol, the reaction pathway of EOR was complicated (Fig. S12).

Fig. 4a and b show the in situ FTIR spectra from −0.9 to 0.1 V. The major bands related to the production or consumption of species were listed in Table S2. The consumption of OH^- species was verified by the two negative bands between 2500 and 2800 and 1700–2000 cm^{-1} (Fig. 4a and b). In combination with the stretching vibration of C-O bond at 1045 cm^{-1}, the deplete of ethanol was confirmed. The $CH_3CH_2O^*$, which was then oxidized to acetate (CH_3COO^-) by OH_{ads}, was the initial intermediate by adsorption of ethanol. The positive bands at 2919 and 2850 cm^{-1} were attributed to C-H stretches of ethoxy ($CH_3CH_2O^*$) adsorbed on the surface of catalyst. For PtCu/Cu_{2-x}Se NWs, at −600 mV, the positive band located at 2329 cm^{-1} was associated with CO_2 symmetric stretching vibration originated from the C-C bond splitting via C1 pathway. The CO_2 dissolved into the alkaline electrolyte and formed CO_3^{2-}, so the band became inconspicuous. In the case of the commercial Pt/C, more acidic intermediate lowered the pH of thin electrolyte layer, thus presenting the band of CO_2 [50]. In both samples, no band of CO (~ 2050 cm^{-1}) was observed. It is because that the C-C bond cleavage could be regarded as an instantaneous process, during which CO_2 produced [51]. Besides, two positive bands at 1546 and 1419 cm^{-1} corresponded to asymmetric and symmetric O-C-O bonds stretching vibrations from the acetate (CH_3COO^-). Due to the overlapping of CO_3^{2-} that located at ~1390 cm^{-1}, the band at 1419 cm^{-1} showed a higher intensity [52]. And the band at 1346 cm^{-1} corresponded to the -CH_3 bending vibrations in acetate. In the in situ FTIR spectra of PtCu/Cu_{2-x}Se NWs, when the potential reached −100 mV, the bands at 1646 cm^{-1} of C═O bonds in acetaldehyde (CH_3CHO) and acetyl (CH_3CO^*) emerged. It indicated that the C-OH formation process from CH_3CHO to CH_3COOH had slowed down, and dehydrogenation process was still going on. The negative band at 1230 cm^{-1} represented the consumption of CH_3CHOH^* -O-Pt, which was an important intermediate of acetate. The bands at 1646 and 1230 cm^{-1} explained that the oxidation of ethanol to acetate was an instantaneous process in a low potential range. As the potential increasing, the C2 pathway was hindered and the generation and consumption of intermediate were observed.

Fig. 4c shows the integral intensities of bands at 1546 and 1419 cm^{-1} corresponding the formation of acetate and carbonate [53,54]. When the voltage raised to −300 mV, the bands of PtCu/Cu_{2-x}Se began to descend, in accord with the appearance of acetaldehyde/acetyl and CH_3CHOH^* -O-Pt. However, the bands of commercial Pt/C declined until reaching 0 V. Therefore, the PtCu/Cu_{2-x}Se NWs had a better capacity of hindering the formation of acetate. Moreover, the band at 1419 cm^{-1} of PtCu/Cu_{2-x}Se NWs became smooth at a higher potential due to the overlapping of carbonate. For PtCu/Cu_{2-x}Se NWs, the integral intensity of band at 1419 cm^{-1} was higher than that at 1546 cm^{-1}, while commercial Pt/C was the opposite. All above results demonstrate

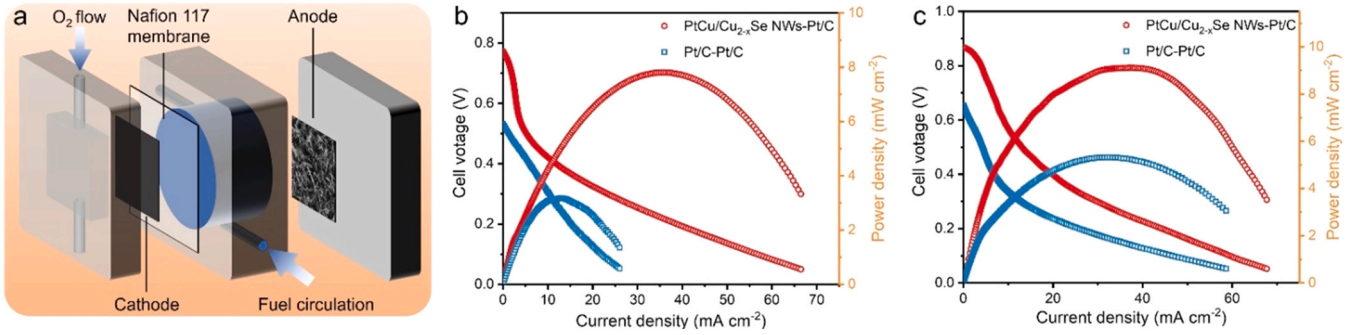

Fig. 5. (a) Schematic diagram of DAFCs. Polarization and power density curves of (b) DEFCs and (c) DMFCs (anode: 4.0 M KOH and 2.0 M ethanol or methanol, cathode: O_2 flow with 10 mL min^{-1}).

that the oxidation of ethanol on PtCu/Cu_{2-x}Se surface is easier to split the C-C bonds to generate CO_3^{2-}.

The C2 product selectivities in EOR were further analyzed. After CV electrolyzing, the electrolytes were collected and quantitatively detected by HPLC. The result showed that acetate and acetaldehyde were identified to be the main oxidation products (Figs. S13 and S14). By comparison of the ratio of integration intensity with standard concentration samples, the concentration of acetate and acetaldehyde in electrolyte are recorded in Table S3. The corresponding faraday efficiency for C2 pathway of PtCu/Cu_{2-x}Se NWs and commercial Pt/C were 30.8% and 52.1%, respectively (Fig. S15) [55]. It suggests that PtCu/Cu_{2-x}Se NWs had a higher C-C cleavage ability to generating C1 products than commercial Pt/C.

DFT calculations were then performed to further describe the catalytic mechanism. A Cu atom in Cu_2Se (111) surface is removed to create surface Cu defects and then a Pt_{13} cluster was placed on the surface to construct PtCu/Cu_{2-x}Se model. The most important intermediates on the Pt_{13}/Cu_{2-x}Se (111) model were calculated and showed in Fig. S16. The depletion of the partial Pt orbitals upon interaction with the surface was observed from the differential charge density plot (Fig. S17). It stayed balanced between the charge density increasing of Pt-Cu and Pt-Se bonds and the surface atoms bonding with the adsorbed Pt atom [56]. Fig. 4d shows the reaction free energy profile of ethanol oxidation based on the computational hydrogen electrode, intermediates below and above the dotted line are due to exothermic and endothermic processes, respectively. Generally, three elementary reaction steps should be considered for the first step of ethanol-electrooxidation under alkaline condition as follows:

The cleavage of O-H:

$$CH_3CH_2OH@cat\cdot \rightarrow CH_3CH_2O^*@cat\cdot + H^+ + e^- \quad (1)$$

The cleavage of α-C-H:

$$CH_3CH_2OH@cat\cdot \rightarrow CH_3CHOH^*@cat\cdot + H^+ + e^- \quad (2)$$

The cleavage of β-C-H:

$$CH_3CH_2OH@cat\cdot \rightarrow CH_2CH_2OH^*@cat\cdot + H^+ + e^- \quad (3)$$

Therefore, the oxidation of ethanol leads to three possible intermediates: $CH_3CH_2O^*$, CH_3CHOH^* (α-hydroxyethyl) and $CH_2CH_2OH^*$ (β-hydroxyethyl). One can see that the α-C-H broken-bond is prior to other two kind of dehydrogenation, which is energetic favorable with the activation energy of 0.16 eV. The intermediates of the first oxidation-step were further dehydrogenated with removing a H^+ and an e^- to form CH_3CHO, CH_2CHOH^* and CH_3COH^*. It is worth noting that CH_2CHOH^* is the predominant precursor for C-C bond splitting [57], so that this reaction route could go further to generate one-carbon intermediates (CO_{ads} and $CH_{x,ads}$) and finally oxidated to CO_2. Besides, the intermediate $CH_3CH(OH)_2^*$ was formed by the addition of OH^- group into CH_3CHOH^* to get C-OH bond. During the process of C-OH formation, the OH^- group was adsorbed on Pt atom, and CH_3CHOH^* -O-Pt acted as the intermediate was observed in the in situ FTIR spectra of PtCu/Cu_{2-x}Se NWs.

To demonstrate the universality of PtCu/Cu_{2-x}Se NWs in alcohol oxidation reaction, the EOR in acid media and MOR in alkaline media were measured. For EOR in acid media (Fig. S18a-c), the MAs of PtCu/Cu_{2-x}Se NWs and commercial Pt/C were fallen to 1617 and 609 mA mg^{-1}_{Pt}, respectively. It is obvious that the PtCu/Cu_{2-x}Se NWs exhibit more excellent catalytic activity in alkaline media. It can be seen that the PtCu/Cu_{2-x}Se NWs showed a highest MA among the recently reported Pt-based catalysts (Fig. S19). The detailed comparison in literature were shown in Table S5. For MOR in alkaline media (Fig. S18d-f), the variation trend of CV curves was similar toward EOR. The MA of PtCu/Cu_{2-x}Se NWs (5.29 A mg^{-1}_{Pt}) was still greater than that of Pt NPs/C (1.34 A mg^{-1}_{Pt}) and commercial Pt/C (1.03 A mg^{-1}_{Pt}). The peak current of backward scans was obvious lower than that of EOR, owing to the unitary intermediates of MOR, multiple dehydrogenation and oxidation of EOR [58]. The CA curves (Fig. S18c) confirmed the durability of these catalysts. After electrolyzing for 1 h, the retained MAs were 415 mA mg^{-1}_{Pt} for PtCu/Cu_{2-x}Se NWs, 134 mA mg^{-1}_{Pt} for Pt NPs/C, and 66 mA mg^{-1}_{Pt} for commercial Pt/C.

Finally, the membrane electrodes were assembled (Fig. 5a). Fig. 5b and c show the performance of the DAFCs with commercial Pt/C as cathode for the oxygen reduction reaction. The DEFCs with PtCu/Cu_{2-x}Se NWs anode provided an open-circuit voltage (OCV) of 0.773 V, which was 240 mV higher than that of Pt/C. And the peak value of power density reached 7.8 mW cm^{-2}, which was 2.5 times higher than that of Pt/C. The DMFCs with PtCu/Cu_{2-x}Se NWs anode also displayed 210 mV higher OCV and 1.7 times higher peak power density than that of Pt/C. The DEFC voltage was collected at a constant current density of 10 mA cm^{-2} for 60 h. Overall, except a few fluctuations, the cell voltage with PtCu/Cu_{2-x}Se NWs anode only showed a slight decline (Fig. S20a) [59]. However, the cell voltage with Pt/C anode dropped by over 50% after 35 h. For DMFCs (Fig. S20b), the cell voltage with PtCu/Cu_{2-x}Se NWs anode was also more stable than that with Pt/C anode. Overall, both the catalytic activity and stability of PtCu/Cu_{2-x}Se NWs outperform the commercial Pt/C, which make it promising for alkaline DAFCs.

3. Conclusion

In summary, benefiting from the PtCu alloy and abundant surface defects, PtCu/Cu_{2-x}Se NWs showed a remarkable activity for both EOR and MOR. The intermediates and the products of ethanol oxidation were analyzed through ex situ, in situ characteristics and DFT calculation. PtCu/Cu_{2-x}Se NWs displayed higher efficiency to break C-C bond to produce more C1 intermediates than commercial Pt/C to oxidize ethanol to CO_2. The assembled DEFCs with PtCu/Cu_{2-x}Se NWs as anode provided an open-circuit voltage (OCV) of 0.773 V and a peak power density of 7.8 mW cm^{-2}. This work gives us a potential catalyst for C-C bond cleavage, and presents an effective strategy to enhance the

electrocatalytic activity of ethanol/methanol oxidation.

CRediT authorship contribution statement

Yongpeng Lei: initiated the project and wrote the manuscript. **Hongcheng Peng:** carried out experiments and wrote the manuscript. **Ren Jun:** carried out the theoretical calculations. **Yuchao Wang:** analyzed the literature and wrote the manuscript. **Yu Xiong:** analyzed the in situ FTIR results. **Qichen Wang:** analyzed the literature and processed the Figures. **Qian Li, Xin Zhao, and Longsheng Zhan:** processed the Figures and polished the language. **Lirong Zheng:** analyzed the synchrotron radiation results. **Yougen Tang:** discussed the experimental results and analyzed the literature.

Declaration of Competing Interest

The authors declare that they have no known competing financial interests or personal relationships that could have appeared to influence the work reported in this paper.

Acknowledgements

The authors gratedfully acknowledge the financial support from the Hunan Provincial Science and Technology Plan Project, China (No. 2017TP1001). Hongcheng Peng thanks the Postdoctoral Research Plan Project in Central South University, China (Grant No. 140050023). The authors acknowledge the 1W1B station for XAFS measurement in the Beijing Synchrotron Radiation Facility (BSRF).

Appendix A. Supporting information

Supplementary data associated with this article can be found in the online version at doi:10.1016/j.nanoen.2021.106307.

References

[1] Y. Yang, M. Luo, W. Zhang, Y. Sun, X. Chen, S. Guo, Metal surface and interface energy electrocatalysis: fundamentals, performance engineering, and opportunities, Chem 4 (2018) 2054–2083.
[2] X. Yang, Q. Wang, S. Qing, Z. Gao, X. Tong, N. Yang, Modulating electronic structure of an Au-nanorod-core-PdPt-alloy-shell catalyst for efficient alcohol electro-oxidation, Adv. Energy Mater. (2021), https://doi.org/10.1002/aenm.202100812.
[3] S. Liu, X. Wang, H. Yu, Y. Wu, B. Li, Y. Lan, T. Wu, J. Zhang, D. Li, Two new pseudo-isomeric nickel (II) metal-organic frameworks with efficient electrocatalytic activity toward methanol oxidation, Rare Met. 40 (2021) 489–498.
[4] Y. Liu, Q. Feng, W. Liu, Q. Li, Y. Wang, B. Liu, L. Zheng, W. Wang, L. Huang, L. Chen, X. Xiong, Y. Lei, Boosting interfacial charge transfer for alkaline hydrogen evolution via rational interior Se modification, Nano Energy 81 (2021), 105641.
[5] Y. Zhang, X. Yuan, F. Lyu, X. Wang, X. Jiang, M. Cao, Q. Zhang, Facile one-step synthesis of PdPb nanochains for high-performance electrocatalytic ethanol oxidation, Rare Met. 39 (2020) 792–799.
[6] Z. Liang, L. Song, S. Deng, Y. Zhu, E. Stavitski, R.R. Adzic, J. Chen, J. Wang, Direct 12-electron oxidation of ethanol on a ternary Au(core)-PtIr(shell) electrocatalyst, J. Am. Chem. Soc. 141 (2019) 9629–9636.
[7] B. Fang, L. Feng, PtCo-NC catalyst derived from the pyrolysis of Pt-incorporated ZIF-67 for alcohols fuel electrooxidation, Acta Phys. Chim. Sin. 36 (2020) 1905023–1905029.
[8] T.W. Deelen, C.H. Mejía, K.P. Jong, Control of metal-support interactions in heterogeneous catalysts to enhance activity and selectivity, Nat. Catal. 2 (2019) 955–970.
[9] C. Lei, W. Zhou, Q. Feng, Y. Lei, Y. Zhang, Y. Chen, J. Qin, Charge engineering of Mo_2C@defect-rich N-doped carbon nanosheets for efficient electrocatalytic H_2 evolution, Nano-Micro Lett. 11 (2019) 45.
[10] F. Lyu, M. Cao, A. Mahsud, Q. Zhang, Interfacial engineering of noble metals for electrocatalytic methanol and ethanol oxidation, J. Mater. Chem. A 8 (2020) 15445–15457.
[11] S. Furukawa, T. Komatsu, Intermetallic compounds: promising inorganic materials for well-structured and electronically modified reaction environments for efficient catalysis, ACS Catal. 7 (2017) 735–765.
[12] L. Chen, X. Liang, X. Li, J. Pei, H. Lin, D. Jia, W. Chen, D. Wang, Y. Li, Promoting electrocatalytic methanol oxidation of platinum nanoparticles by cerium modification, Nano Energy 73 (2020), 104784.
[13] T. Wang, F. Li, H. Huang, S. Yin, P. Chen, P. Jin, Y. Chen, Porous Pd-PdO nanotubes for methanol electrooxidation, Adv. Funct. Mater. 30 (2020), 2000534.
[14] S. Zhang, C. Sun, J. Zeng, Q. Sun, G. Wang, Y. Wang, Y. Wu, S. Dou, M. Gao, Z. Li, Ambient aqueous synthesis of ultrasmall PEGylated Cu_{2-x} Se nanoparticles as a multifunctional theranostic agent for multimodal imaging guided photothermal therapy of cancer, Adv. Mater. 28 (2016) 8927–8936.
[15] Z. Zhai, K. Huang, X. Wu, Superior mixed Co-Cd selenide nanorods for high performance alkaline battery-supercapacitor hybrid energy storage, Nano Energy 47 (2018) 89–95.
[16] Z. Ali, M. Asif, T. Zhang, X. Huang, Y. Hou, General approach to produce nanostructured binary transition metal selenides as high-performance sodium ion battery anodes, Small 15 (2019), 1901995.
[17] Q. Wang, Y. Lei, D. Wang, Y. Li, Defect engineering in earth-abundant electrocatalysts for CO_2 and N_2 reduction, Energy Environ. Sci. 12 (2019) 1730–1750.
[18] L. Tao, Y. Shi, Y. Huang, R. Chen, Y. Zhang, J. Huo, Y. Zou, G. Yu, J. Luo, C. Dong, S. Wang, Interface engineering of Pt and CeO_2 nanorods with unique interaction for methanol oxidation, Nano Energy 53 (2018) 604–612.
[19] Z. Chen, Q. Wang, X. Zhang, Y. Lei, W. Hu, Y. Luo, Y. Wang, N-doped defective carbon with trace Co for efficient rechargeable liquid electrolyte-/all-solid-state Zn-air batteries, Sci. Bull. 63 (2018) 548–555.
[20] J. Xu, W. Zhang, Z. Yang, S. Ding, C. Zeng, L. Chen, Q. Wang, S. Yang, Large-scale synthesis of long crystalline $Cu_{2-x}Se$ nanowire bundles by water-evaporation-induced self-assembly and their application in gas gensing, Adv. Funct. Mater. 19 (2009) 1759.
[21] L. Xiao, G. Li, Z. Yang, K. Chen, R. Zhou, H. Liao, Q. Xu, J. Xu, Engineering of amorphous PtO_x interface on Pt/WO_3 nanosheets for ethanol oxidation electrocatalysis, Adv. Funct. Mater. (2021), https://doi.org/10.1002/adfm.202100982.
[22] Z. Wu, Y. Zhao, W. Jin, B. Jia, J. Wang, T. Ma, Recent progress of vacancy engineering for electrochemical energy conversion related applications, Adv. Funct. Mater. 31 (2021), 2009070.
[23] Q. Wang, X. Xue, Y. Lei, Y. Wang, Y. Feng, X. Xiong, Di Wang, Y. Li, Engineering of electronic states on Co_3O_4 ultrathin nanosheets by cation substitution and anion vacancies for oxygen evolution reaction, Small 16 (2020), 2001571.
[24] J. Bai, X. Xiao, Y. Xue, J. Jiang, J. Zeng, X. Li, Y. Chen, Bimetallic platinum-rhodium alloy nanodendrites as highly active electrocatalyst for the ethanol oxidation reaction, ACS Appl. Mater. Interfaces 11 (2018) 19755–19763.
[25] Z. Li, J. Fu, Y. Feng, C. Dong, H. Liu, X. Du, A silver catalyst activated by stacking faults for the hydrogen evolution reaction, Nat. Catal. 2 (2019) 1107–1114.
[26] C. Wu, H. Li, H. He, Y. Song, C. Bi, W. Du, H. Xia, Compressive strain in core-shell Au-Pd nanoparticles introduced by lateral confinement of deformation twinnings to enhance the oxidation reduction reaction performance, ACS Appl. Mater. Interfaces 11 (2019) 46902–46911.
[27] C. Zhang, Y. Shi, Y. Yu, Y. Du, B. Zhang, Engineering sulfur defects, atomic thickness, and porous structures into cobalt sulfide nanosheets for efficient electrocatalytic alkaline hydrogen evolution, ACS Catal. 8 (2018) 8077–8083.
[28] C. Choi, T. Cheng, M.F. Espinosa, H. Fei, X. Duan, W.A. Goddard III, Y. Huang, A highly active star decahedron Cu nanocatalyst for hydrocarbon production at low overpotentials, Adv. Mater. 31 (2019), 1805405.
[29] Y. Chen, S. Ji, W. Sun, W. Chen, J. Dong, J. Wen, J. Zhang, Z. Li, L. Zheng, C. Chen, Q. Peng, D. Wang, Y. Li, Discovering partially charged single-atom Pt for enhanced anti-Markovnikov alkene hydrosilylation, J. Am. Chem. Soc. 140 (2018) 7407–7410.
[30] G. Song, Y. Wang, Y. Qi, W. Li, L. Zhang, Fabrication of titanium nitride nanoparticles onto carbon nanotubes by atomic layer deposition for utilization as Pt electrocatalyst supports, Rare Met. 39 (2020) 784–791.
[31] Y. Xiong, P. Xin, W. Chen, Y. Wang, S. Zhang, H. Ren, H. Rong, X. Zheng, C. Chen, Q. Peng, D. Wang, Y. Li, PtAl truncated octahedron nanocrystals for improved formic acid electrooxidation, Chem. Commun. 54 (2018) 3951–3954.
[32] X. Yuan, W. Yue, J. Zhang, Electrochemically exfoliated graphene as high-performance catalyst support to promote electrocatalytic oxidation of methanol on Pt catalysts, J. Cent. South. Univ. 27 (2020) 2515–2529.
[33] J. Kim, W. Choi, J.W. Park, C. Kim, M. Kim, H. Song, Branched copper oxide nanoparticles induce highly selective ethylene production by electrochemical carbon dioxide reduction, J. Am. Chem. Soc. 141 (2019) 6986–6994.
[34] H. Jung, S.Y. Lee, C.W. Lee, M.K. Cho, D.H. Won, C. Kim, H.S. Oh, B.K. Min, Y. J. Hwang, Electrochemical fragmentation of Cu_2O nanoparticles enhancing selective C-C coupling from CO_2 reduction reaction, J. Am. Chem. Soc. 141 (2019) 4624–4633.
[35] K. Jiang, M. Luo, M. Peng, Y. Yu, Y. Lu, T. Chan, P. Liu, F.M.F. de Groot, Y. Tan, Dynamic active-site generation of atomic iridium stabilized on nanoporous metal phosphides for water oxidation, Nat. Commun. 11 (2020) 2701.
[36] L. Ma, X. Luo, A.J. Kropf, J. Wen, X. Wang, S. Lee, D.J. Myers, D. Miller, T. Wu, J. Lu, K. Amine, Insight into the catalytic mechanism of bimetallic platinum-copper core-shell nanostructures for nonaqueous oxygen evolution reactions, Nano Lett. 16 (2016) 781–785.
[37] T. Chao, X. Luo, W. Chen, B. Jiang, J. Ge, Y. Lin, G. Wu, X. Wang, Y. Hu, Z. Zhuang, Y. Wu, X. Hong, Y. Li, Atomically dispersed copper-platinum dual sites alloyed with palladium nanorings catalyze the hydrogen evolution reaction, Angew. Chem. Int. Ed. 56 (2017) 16047–16051.
[38] Y. Qu, B. Chen, Z. Li, X. Duan, L. Wang, Y. Lin, T. Yuan, F. Zhou, Y. Hu, Z. Yang, C. Zhao, J. Wang, C. Zhao, Y. Hu, G. Wu, Q. Zhang, Qi Xu, B. Liu, P. Gao, R. You, W. Huang, L. Zheng, L. Gu, Y. Wu, Y. Li, Thermal emitting strategy to synthesize atomically dispersed Pt metal sites from bulk Pt metal, J. Am. Chem. Soc. 141 (2019) 4505–4509.
[39] Z. Luo, Y. Ouyang, H. Zhang, M. Xiao, J. Ge, Z. Jiang, J. Wang, D. Tang, X. Cao, C. Liu, W. Xing, Chemically activating MoS_2 via spontaneous atomic palladium

interfacial doping towards efficient hydrogen evolution, Nat. Commun. 9 (2018) 2120.
[40] X. Sun, D. Li, Y. Ding, W. Zhu, S. Guo, Z.L. Wang, S. Sun, Core/shell Au/CuPt nanoparticles and their dual electrocatalysis for both reduction and oxidation reactions, J. Am. Chem. Soc. 136 (2014) 5745–5749.
[41] Q. Yun, Q. Lu, C. Li, B. Chen, Q. Zhang, Q. He, Z. Hu, Z. Zhang, Y. Ge, N. Yang, J. Ge, Y. He, L. Gu, H. Zhang, Synthesis of PdM (M = Zn, Cd, ZnCd) nanosheets with an unconventional face-centered tetragonal phase as highly efficient electrocatalysts for ethanol oxidation, ACS Nano 13 (2019) 14329–14336.
[42] L.L. Carvalho, F. Colmati, A.A. Tanaka, Nickel-palladium electrocatalysts for methanol, ethanol, and glycerol oxidation reactions, Int. J. Hydrogen Energy 42 (2017) 16118–16126.
[43] P. Yang, X. Yuan, H. Hu, Y. Liu, H. Zheng, D. Yang, L. Chen, M. Cao, Y. Xu, Y. Min, Y. Li, Q. Zhang, Solvothermal synthesis of alloyed PtNi colloidal nanocrystal clusters (CNCs) with enhanced catalytic activity for methanol oxidation, Adv. Funct. Mater. 28 (2018), 1704774.
[44] Q. Wang, Z. Zhao, Y. Jia, M. Wang, W. Qi, Y. Pang, J. Yi, Y. Zhang, Z. Li, Z. Zhang, Unique Cu@CuPt core-shell concave octahedron with enhanced methanol oxidation activity, ACS Appl. Mater. Interfaces 9 (2017) 36817–36827.
[45] J. Mao, W. Chen, D. He, J. Wan, J. Pei, J. Dong, Y. Wang, P. An, Z. Jin, W. Xing, H. Tang, Z. Zhuang, X. Liang, Y. Huang, G. Zhou, L. Wang, D. Wang, Y. Li, Design of ultrathin Pt-Mo-Ni nanowire catalysts for ethanol electrooxidation, Sci. Adv. 3 (2017), 1603068.
[46] H. Peng, W. Qi, H. Wu, J. He, Y. Li, H. Xie, One-pot synthesis of CuPt nanodendrites with enhanced activity towards methanol oxidation reaction, RSC Adv. 8 (2018) 9293–9298.
[47] M. Li, K. Duanmu, C. Wan, T. Cheng, L. Zhang, S. Dai, W. Chen, Z. Zhao, P. Li, H. Fei, Y. Zhu, R. Yu, J. Luo, K. Zang, Z. Lin, M. Ding, J. Huang, H. Sun, J. Guo, X. Pan, W.A. Goddard III, P. Sautet, Y. Huang, X. Duan, Single-atom tailoring of platinum nanocatalysts for high-performance multifunctional electrocatalysis, Nat. Catal. 2 (2019) 495–503.
[48] P. Ge, S. Li, L. Xu, K. Zou, X. Gao, X. Cao, G. Zou, H. Hou, X. Ji, Hierarchical hollow-microsphere metal-selenide@carbon composites with rational surface engineering for advanced sodium storage, Adv. Energy Mater. 9 (2019), 1803035.
[49] V. Lesnyak, R. Brescia, G.C. Messina, L. Manna, Cu vacancies boost cation exchange reactions in copper selenide nanocrystals, J. Am. Chem. Soc. 137 (2015) 9315–9323.
[50] P.A. Christensen, S.W.M. Jones, An in situ FTIR study of ethanol oxidation at polycrystalline platinum in 0.1 M KOH at 25 and 50 °C, J. Phys. Chem. C 118 (2014) 29760–29769.
[51] E.A. Monyoncho, S.N. Steinmann, C. Michel, E.A. Baranova, T.K. Woo, P. Sautet, Ethanol electro-oxidation on palladium revisited using polarization modulation enfrared reflection absorption spectroscopy (PM-IRRAS) and density functional theory (DFT): why is it difficult to break the C-C Bond? ACS Catal. 6 (2016) 4894–4906.
[52] F. Lv, W. Zhang, M. Sun, F. Lin, T. Wu, P. Zhou, W. Yang, P. Gao, B. Huang, S. Guo, Au clusters on Pd nanosheets selectively switch the pathway of ethanol electrooxidation: amorphous/crystalline interface matters, Adv. Energy Mater. 11 (2021), 2100187.
[53] J. Guo, R. Chen, F. Zhu, S. Sun, H.M. Villullas, New understandings of ethanol oxidation reaction mechanism on Pd/C and Pd_2Ru/C catalysts in alkaline direct ethanol fuel cells, Appl. Catal. B 224 (2018) 602–611.
[54] J. Li, S.Z. Jilani, H. Lin, X. Liu, K. Wei, Y. Jia, P. Zhang, M. Chi, Y.J. Tong, Z. Xi, S. Sun, Ternary CoPtAu nanoparticles as a general catalyst for highly efficient electro-oxidation of liquid fuels, Angew. Chem. Int. Ed. 58 (2019) 11527–11533.
[55] W. Huang, X. Ma, H. Wang, R. Feng, J. Zhou, P.N. Duchesne, P. Zhang, F. Chen, N. Han, Zhao, J. Zhou, W. Cai, Y. Li, Promoting effect of $Ni(OH)_2$ on palladium nanocrystals leads to greatly improved operation durability for electrocatalytic ethanol oxidation in alkaline solution, Adv. Mater. 29 (2017), 1703057.
[56] F. Gao, J. Ren, Q. Wang, D. Li, B. Hou, L. Jia, D. Cao, Theoretical insight into cobalt subnano-clusters adsorption on α-Al_2O_3 (0001), J. Solid State Chem. 246 (2017) 176–185.
[57] B. Zhang, W. Lai, T. Sheng, X. Qu, Y. Wang, L. Ren, L. Zhang, Y. Du, Y. Jiang, S. Sun, S. Dou, Ordered platinum-bismuth intermetallic clusters with Pt-skin for a highly efficient electrochemical ethanol oxidation reaction, J. Mater. Chem. A 7 (2019) 5214–5220.
[58] Y. Ma, L. Yin, T. Yang, Q. Huang, M. He, H. Zhao, D. Zhang, M. Wang, Z. Tong, One-pot synthesis of concave platinum-cobalt nanocrystals and their superior catalytic performances for methanol electrochemical oxidation and oxygen electrochemical reduction, ACS Appl. Mater. Interfaces 9 (2017) 36164–36172.
[59] Y. Feng, H. Liu, J. Yang, A selective electrocatalyst-based direct methanol fuel cell operated at high concentrations of methanol, Sci. Adv. 3 (2017), 1700580.